Title **The Biaxial Strain Dependence of Magnetic Order in Spin Frustrated Mn_3NiN Thin Films**

Author(s), and Corresponding Author(s)* *David Boldrin*, Freya Johnson, Ryan Thompson, Andrei P. Mihai, Bin Zou, Jan Zemen, Jack Griffiths, Patrik Gubeljak, Kristian L. Ormandy, Pascal Manuel, Dmitry D. Khalyavin, Bachir Ouladdiaf, Navid Qureshi, Peter Petrov, Will Branford and Lesley F. Cohen*

Dr. D. Boldrin, F. Johnson, J. Griffiths, P. Gubeljak, K. L. Ormandy, R. Thompson, Dr. W. Branford
Department of Physics, Imperial College London, London, SW7 2AZ, UK
E-mail: d.boldrin@imperial.ac.uk
Dr. J. Zemen
Faculty of Electrical Engineering, Czech Technical University in Prague, Technická 2, Prague 166 27, Czech Republic
Dr. A. P. Mihai, Dr. B. Zou, Dr. P. Petrov
Department of Materials, Imperial College London, London, SW7 2AZ, UK
Dr. P. Manuel, Dr. D. Khalyavin
STFC Rutherford Appleton Lab, ISIS Facility, Harwell Science and Innovation Campus, Didcot, OX11 0QX, United Kingdom
Dr. B. Ouladdiaf, Dr. N. Qureshi
Institut Laue-Langevin, 71 avenue des Martyrs, CS 20156, 38042 Grenoble Cedex 9, France
Prof. L. F. Cohen
Department of Physics, Imperial College London, London, SW7 2AZ, UK

Keywords: piezomagnetism; antiperovskite; ; antiferromagnet; spintronics, frustration

Multi-component magnetic phase diagrams are a key property of functional materials for a variety of uses, such as manipulation of magnetisation for energy efficient memory, data storage and cooling applications. Strong spin-lattice coupling extends this functionality further by allowing electric-field-control of magnetisation via strain coupling with a piezoelectric . Here we explore the magnetic phase diagram of piezomagnetic Mn_3NiN thin films, with a frustrated non-collinear antiferromagnetic (AFM) structure, as a function of the growth induced biaxial strain. Under compressive strain the films support a canted AFM state with large coercivity of the transverse anomalous Hall resistivity, ρ_{xy}, at low temperature, that transforms at a well-defined Néel transition temperature (T_N) into a soft ferrimagnetic-like (FIM) state at high temperatures. In stark contrast, under tensile strain the low temperature canted AFM phase transitions to a state where ρ_{xy} is an

order of magnitude smaller and therefore consistent with a low magnetisation phase. Neutron scattering confirms that the high temperature FIM-like phase of compressively strained films is magnetically ordered and the transition at T_N is 1st-order. Our results open the field towards future exploration of electric-field driven piezospintronic and thin film caloric cooling applications in both Mn_3NiN itself and the broader Mn_3AN family.

Functional properties of antiferromagnets (AFM) are attracting increased attention, most notably for their rich topological properties [1–3] and applications as active elements in memory devices [4–6]. Additional functionality can be achieved in AFMs when multiple magnetic phases can be accessed via an easily controllable parameter, such as lattice strain, where strong magnetostructural coupling drives sharp changes in the magnetism. For instance, the topologically enhanced anomalous Hall effect (AHE) in Mn_3Pt can be switched using electric field due to a 1st-order AFM-AFM transition [7]. Similarly, the 1st-order AFM-ferromagnetic (FM) transition in FeRh has been utilised to allow magnetisation switching at room temperature [8], meaning it can be used as a memory resistor [9], as well as in a caloric cooling cycle [10]. However, only a handful of materials are known where such functionality exists, particularly in thin film form and applicable at room temperature.

Manganese nitride antiperovskites (Mn_3AN) display a range of intriguing properties such as zero-coefficient of resistivity [11], anomalous thermal expansion [12], barocaloric [13,14], and piezospintronic effects [15–18]. The latter relates to piezomagnetism, a linear magnetostructural coupling effect whereby a finite magnetisation can be produced and manipulated by changing the biaxial lattice strain in zero magnetic field [15,16,19–21]. Recent prediction suggests a rich magnetic phase diagram in Mn_3GaN accessible by varying biaxial strain, with remarkably different magnetic states accesible [19]. Through coupling to a piezoelectric, the piezomagnetic effect in these materials has the potential to provide large and reversible electric-field driven changes in magnetisation, a long sought-after goal of multiferroic and spintronics research [22] as well as thin film calorics [8,10,23,24].

The driving force behind these properties is the strong magnetostructural coupling due to geometrically frustrated exchange interactions [12,16]. The frustration leads to non-collinear AFM structures in several members of the Mn_3AN family, in particular two fully compensated structures we term Γ_{4g} and Γ_{5g} [25]; **Figure 1a** shows the Γ_{4g} structure, whilst Γ_{5g} in **Figure 1b** is obtained by rotating all spins by 90° in the (111) plane. Interestingly, the magnetic frustration in the Mn_3AN family is closely related to the more widely studied cubic Mn_3X compounds where giant anomolous Hall [1,26] and magneto-optical Kerr effects [3,27] have been predicted and observed. The magnetic structure in Mn_3AN are most closely related to the cubic Mn_3X analogues with X = Rh, Pt, Ir [28,29], which order at low temperatures in the non-collinear antiferromagnetic Γ_{4g} structure in addition to a high temperature collinear antiferromagnetic phase.

The temperature-biaxial strain magnetic phase diagram predicted in Mn_3GaN is derived from the Γ_{5g} magnetic structure of the unstrained material (see **Figure 1b**) [19]. Motivated by this work and the lack of experimental verification, here we choose to study the temperature-biaxial-strain phase diagram in thin films of the closely related antiperovskite Mn_3NiN, using the anomalous Hall effect (AHE), magnetometry and neutron scattering. The magnetic structure of unstrained Mn_3NiN predominantly adopts the Γ_{4g} magnetic structure close to the Néel temperature, T_N = 260K [14,25]. Taking the predicted structures induced by biaxial strain in Mn_3GaN, a 90º rotation of all spins in the (111) plane leads to similar collinear ferri- and antiferromagnetic phases derived from the Γ_{4g} magnetic structure, see **Figure 1c** and **1d**. Accordingly, we find quite striking differences when Mn_3NiN films are grown under compressive or tensile strain, particularly with respect to their magnetic properties above T_N, in agreement with these predictions

Conventionally, the Hall resistivity is defined by $\rho_{xy} = R_o\mu_0 H + R_s\mu_0 M$ where R_o and R_s are the normal and AHE contributions, respectively, and M is the magnetisation. Thus, due to the out-of-plane magnetisation of our strained Mn_3NiN films [20], we expect ρ_{xy} to include a measurable

AHE contribution. Additionally, a further intrinsic contribution to the AHE arises when the films adopt the Γ_{4g} non-collinear magnetic structure, due to the Berry curvature associated with its band structure [30]. To estimate the normal Hall contribution we use DFT calculations at zero temperature of the carrier density as 2.4×10^{21} cm^{-3}, which gives a normal Hall contriubition $R_{o,th}$ = 26×10^{-2} μΩcm/T. **Figure 1e** shows the estimated normal Hall contribution, $R_{o,th}H$, which approximately accounts for the unsaturated contribution of ρ_{xy} at high magnetic fields. The films show typical metallic-like behaviour of the longitudinal resistivity (ρ_{xx}) upon warming from low temperature followed by a plateau above T_N (see **Figure S1a**), similar to bulk Mn_3NiN [31]. Further structural details of the films employed are listed in **Table S1**.

Figures 1e and **1f** shows ρ_{xy} for films with large (> 0.1%) compressive (100nm on $SrTiO_3$ (STO), #4) and tensile (50nm on $(LaAlO_3)_{0.3}(Sr_2TaAlO_6)_{0.7}$ (LSAT), #1) biaxial strains, respectively, above and below their respective T_N. Above T_N, the compressively strained film shows a large soft ferrimagnetic (FIM)-like response with zero hysteresis, whilst in contrast ρ_{xy} of the film with tensile strain is reduced by an order of magnitude. Below T_N ρ_{xy} has finite hysteresis in both films and does not fully saturate upto large fields. In order to estimate the field saturated value of the Hall resistivity, $\rho_{xy,sat}$, a linear extrapolation is taken from the high field region of ρ_{xy} to the value at $H = 0$, indicated in **Figure 1e**. The slope of this fit we assign to R_o.

The temperature dependence of R_o, the extracted H_C and $\rho_{xy,sat}$ for each of the films is shown in **Figure 1g-1i** against the reduced temperature, T/T_N. It is interesting that the change in R_o, ΔR_o, at T_N can take either positive or negative sign, suggesting that the high field slope responds to more complex changes than the carrier density extracted from a single carrier model. Either way we associate ΔR_o at T_N to be indicative of a sharp first-order like transition. A similar jump is found in $\rho_{xx}(T)$ of bulk Mn_3NiN at T_N where in this case it is well established that the transition is strongly first-order with a 0.4% coupled volume change [31]. Noticeably, all films show a sharp change in R_o at T_N except the 10nm on STO (#5) where the transition is smooth.

Compressive (STO) and tensile (LSAT) strained films show striking differences in $\rho_{xy,sat}$ around T_N (see **Figure 1h**). For films on LSAT $\rho_{xy,sat}$ significantly decreases upon warming above T/T_N ~ 0.5, whilst for those on STO $\rho_{xy,sat}$ remains relatively constant either side of T_N. In the 10nm film on STO (#5) $\rho_{xy,sat}$ changes by only 10% between 2 and 280K, less than the thicker 100nm film. For the films grown on $BaTiO_3$ (BTO), where the substrate lattice parameter is significantly larger than Mn_3NiN and therefore the film growth is not purely epitaxial, the behaviour of $\rho_{xy,sat}$ for the two films is quite different. For film #6 on BTO, where the lattice parameter and transition temperature suggest the film is compressively strained (see **Table S1** and **Figure S2**), $\rho_{xy,sat}$ is large above T_N and reduces gradually below T_N, which is comparable to films on STO. For film #3, where the lattice parameter and transition temperature is roughly the same as the bulk (see **Table 1** and **Figure S2**), $\rho_{xy,sat}$ is small above T_N and increases upon cooling. This behaviour is similar to that found for films on LSAT (#1 and #2), however even for zero strain one expects a significant AHE arising from the Γ_{4g} structure [30].

The magnetism can also be parameterised by the coercive field, H_C, defined in **Figure 1e** and shown in **Figure 1i** as a function of the reduced temperature. All films show zero H_C above T_N and finite coercivity below it. As with $\rho_{xy,sat}$, it is evident that for films with opposite strain, H_C behaves quite differently. For the 10nm film on STO (#5), H_C increases gradually and does not saturate as T approaches zero suggestive of a continuous transition, whilst for both films on LSAT (#1 and #2) H_C increases sharply and either saturates or decreases again at low temperatures. A change of transition from 1st-order to continuous behaviour as a function of strain has also been predicted in the Mn_3GaN [19], although for opposite sign strains.

In both $\rho_{xy,sat}$ and H_C we can identify three clear regimes of behaviour: (i) the regime above T_N, where films under compressive and tensile strain show large and small AHE, respectively; (ii) the intermediate temperature regime below T_N, which is consistent with contributions to the AHE from the Γ_{4g} magnetic structure [30]; (iii) a low temperature regime where all films show a decrease in $\rho_{xy,sat}$, generally below $T/T_N < 0.5$. This latter feature is most marked in the LSAT

100nm film (#2, see **Figure S1b**); upon cooling below 100K the coupling of ρ_{xy} to the field weakens and reduces the coercivity. At lowest temperatures the behaviour resembles the magnetisation of an antiferromagnet that is weakly coupled to the field, behaviour closely resembling the compensated non-collinear antiferromagnetic Γ_{5g} structure of bulk samples.

We now discuss the magnetic anisotropy of our Mn_3NiN thin films. The net magnetisation piezomagnetically induced by biaxial strain in the Γ_{5g} and Γ_{4g} magnetic structures lies along different directions within the (111) plane, specifically the [110] axis in the former and the [112] axis in the latter. Therefore, in samples grown along the [001] axis one would expect different anisotropies for the two magnetic structures; for Γ_{4g} the magnetisation should have approximately equal components in- (IP) and out-of-plane (OOP), whereas for Γ_{5g} the applied field is expected to couple to the magnetisation IP resulting in a soft magnetic component.

The magnetic anisotropy of compressive and tensile films is quite different (see **Figures 2a-d**). At all temperatures film #1 on LSAT shows strongly anistropic behaviour with the easy axis lying IP. Upon subtracting the low field jump from the IP data the $M(H)$ loop overlays the OOP data and the area of the hysteresis loops are equal for IP and OOP shown in **Figure S3**. This behaviour can be understood by appreciating that a strained Γ_{5g} magnetic structure will have an uncompensated moment lying in the IP direction [19], enabling manipulation of the spin for in-plane applied magnetic fields. The anisotropy of films on STO is quite different, both IP and OOP magnetometry match closely at all temperatures, entirely consistent with the Γ_{4g} magnetic structure [20]. The magnetometry data indicates that the magnetic structure consists of mixed ratios of Γ_{4g} and Γ_{5g} and whilst biaxial strain may be only one of a number of parameters that controls this ratio it is interesting that the magnetic anisotropies can be so significantly manipulated.

To provide further insight into the magnetic phases above and below T_N in Mn_3NiN thin films, we performed neutron diffraction measurements on a 100nm Mn_3NiN/BTO film (#6) at the WISH and D10 diffractometers at ISIS (UK) and ILL (France), respectively. **Figures 2e-g**

shows the (100), (110) and (200) peaks collected at various temperatures on the WISH diffractomer. The temperature dependence of the film in-plane lattice parameter (which we arbitrarily call the *a*-lattice parameter), determined from the (100) and (200) peaks, is shown in **Figure 2h**. The large increase of the lattice when cooled through T_N is characteristic of Mn_3NiN [14,25] and the magnitude of this change, $\Delta a = 0.7\%$, is in good agreement with the 0.4% measured in the bulk and further evidences that the transition in the film maintains a 1st-order character.

The intensity of the (100) peak has a strong temperature dependence and this is plotted in **Figure 2i** alongside the same data collected on a polycrystalline bulk sample [14] and the dense target used for film growth [32]. At 450K in the paramagnetic regime the intensity is small in all samples, as expected for paramagnetic Mn_3NiN. Upon cooling the intensity from the thin film increases considerably before T_N is reached, in contrast to bulk samples where the intensity only increases below T_N. The (110) peak is expected to have the largest nuclear intensity, however only a broad and weak peak is observed in the film which may suggest that it does not grow well along this direction (see **Figure 2f**). The (200) peak is not apparent in the 450K data, however a weak peak is seen at 300K that increases in intensity upon further cooling to 150K (see **Figure 2g**). Importantly, this peak only has a magnetic contribution in the Γ_{4g} structure (and not Γ_{5g}) with a ferromagnetic component along the (111) direction, i.e. a canting of the spins out of the kagome (111) plane. Taken together, the change of intensity of the (100) and (200) peaks with temperature provides clear evidence that the materials are magnetically ordered both at room temperature and below T_N. Moreover, the presence of magnetic intensity on the (200) peak is consistent with a Γ_{4g} component below T_N.

We now use the acquired $\rho_{xy,sat}$ collected on all films to map the temperature-biaxial strain magnetic phase diagram for piezomagnetic Mn_3NiN, shown in **Figure 3**. We use values of the biaxial strain calculated using the Poisson ratio and *c*-axis lattice parameter for consistency across all films, allowing us to make qualitative comparisons. However, high-resolution

transmission electron miscroscopy (HRTEM) measurements on Film #4 show that the maximum strain may be significantly larger (see Table S1). Whilst the phase diagram predicted for Mn_3GaN is plotted with respect to net magnetisation [19], our phase diagram for Mn_3NiN shares many qualitative similarities: (i) the T_N dependence with strain is in the same direction; (ii) different high and low $\rho_{xy,sat}$ states exist in the opposite strain regimes above T_N; (iii) high $\rho_{xy,sat}$ states exist at low temperature for both compressive and tensile strain; (iv) the transition at T_N becomes 2nd-order-like at large compressive strains, in the opposite sense to Mn_3GaN where large tensile strains result in 2nd-order behaviour [19]. Furthermore, noticeable differences to the Mn_3GaN magnetisation phase diagram are also present: (i) films with small strain show large $\rho_{xy,sat}$ below T_N due to the Berry curvature contribution to the AHE that is allowed despite negligible magnetisation [30]; (ii) a region of low $\rho_{xy,sat}$ exists below T_N for small compressive strain. This may exist because compressive strain is predicted to reduce the AHE [30], however as further compressive strain is applied the net magnetisation due to the piezomagnetism may then act as an additional contribution to the AHE.

Piezoelectric controlled antiferromagnetic-based spintronic devices, 'antiferromagnetic piezospintronics', offer significant advantages over conventional devices. For instance, a non-volatile and magnetic field insensitive memory device has recently been demonstrated in MnPt-based heterostructures [33], whilst in similar Mn_3Pt-based structures the non-collinear AFM state which gives rise to an AHE can be switched piezoelectrically [7]. Given the results presented here for Mn_3NiN, piezoelectric control of the strain in this material would allow access to a number of magnetic states and, therefore, the large associated changes in the AHE (see **Figure 1h**), magnetisation [20] and entropy [19]. The required strains of the order of 0.1% is an order-of-magnitude less than that required in Mn_3GaN, as expected given the larger predicted piezomagnetic effect in Mn_3NiN, and easily within practical limits [7]. Further improvements could be made with thin films of Mn_3SnN, which is predicted to offer a further 5 times increase in the piezomagnetic effect over Mn_3NiN [15] in addition to a high transition temperature, T_N =

450K [34], opening the possibility of room temperature applications. If it is attractive to tailor T_N to room temperature but retain the additional sensitivity offered by Mn_3SnN, it is straightforward to visualise that alloys of Ni and Sn, readily achievable in the bulk, may offer the best combination of T_N and strain sensitivity.

In conclusion, here we examine the magnetic phase diagram of Mn_3NiN as a function of biaxial strain and temperature using the AHE and magnetometry in films grown on different substrates. The films support different magnetic ordering depending on whether they are under in-plane tensile or compressive biaxial strain, particularly in the region of the phase diagram just above T_N. Our observations share strong similarlities with the theoretical prediction for Mn_3GaN [19] although in much smaller strain fields. Our findings inspire further experiments to (i) discover larger effects at room temperature, which could be achieved in thin films of other members of the chemically flexible Mn_3AN, e.g. Mn_3SnN [15,17] and (ii) develop piezoelectrically coupled Mn_3AN thin films in order to transition between these magnetic phases with electric field.

Experimental Section

Thin films of Mn_3NiN were grown by pulsed laser deposition (PLD), as described in detail elsewhere [20]. Properties of the films used in this study are summarised in Table S1. The bulk lattice parameter of the Mn_3NiN target used for growth is 3.8805Å. As we have previously found, growth on [001] oriented SrTiO3 (STO), a = 3.905Å, results in compressive in-plane biaxial strain, whilst on (LaAlO3)0.3(Sr2TaAlO6)0.7 (LSAT), a = 3.868Å, results in tensile in-plane biaxial strain [20]. Similar to STO, on $BaTiO_3$ (BTO), a = 3.990Å, one expects compressive in-plane strain, however given the large difference in the substrate and film lattice (see **Figure S2**) and that the substrate is tetragonal at room temperature, the in-plane strain is not simply a function of the lattice parameter. To calculate the in-plane strain we assume Poisson's ratio υ = 0.41 and $\varepsilon_{xx}/\varepsilon_{zz} = -2\upsilon/(1-\upsilon)$. Four terminal magnetotransport data were collected in a square geometry using the van der Pauw method. Magnetisation measurements were performed with a Quantum Design Physical Property Measurement Systems (PPMS-9T). Neutron diffraction

measurements were performed at the WISH diffractometer at ISIS, UK and the D10 diffractometer at ILL, France.

Acknowledgements

Received: ((will be filled in by the editorial staff))
Revised: ((will be filled in by the editorial staff))
Published online: ((will be filled in by the editorial staff))

References

[1] S. Nakatsuji, N. Kiyohara, T. Higo, *Nature* **2015**, *527*, 212.
[2] M. Ikhlas, T. Tomita, T. Koretsune, M. T. Suzuki, D. Nishio-Hamane, R. Arita, Y. Otani, S. Nakatsuji, *Nat. Phys.* **2017**, *13*, 1085.
[3] T. Higo, H. Man, D. B. Gopman, L. Wu, T. Koretsune, O. M. J. Van 'T Erve, Y. P. Kabanov, D. Rees, Y. Li, M. T. Suzuki, S. Patankar, M. Ikhlas, C. L. Chien, R. Arita, R. D. Shull, J. Orenstein, S. Nakatsuji, *Nat. Photonics* **2018**, *12*, 73.
[4] T. Jungwirth, X. Marti, P. Wadley, J. Wunderlich, *Nat. Nanotechnol.* **2016**, *11*, 231.
[5] A. H. MacDonald, M. Tsoi, *Philos. Trans. R. Soc. A Math. Phys. Eng. Sci.* **2011**, *369*, 3098.
[6] J. Železný, P. Wadley, K. Olejník, A. Hoffmann, H. Ohno, *Nat. Phys.* **2018**, *14*, 220.
[7] Z. Q. Liu, H. Chen, J. M. Wang, J. H. Liu, K. Wang, Z. X. Feng, H. Yan, X. R. Wang, C. B. Jiang, J. M. D. Coey, A. H. MacDonald, *Nat. Electron.* **2018**, *1*, 172.
[8] R. O. Cherifi, V. Ivanovskaya, L. C. Phillips, A. Zobelli, I. C. Infante, E. Jacquet, V. Garcia, S. Fusil, P. R. Briddon, N. Guiblin, A. Mougin, A. A. Ünal, F. Kronast, S. Valencia, B. Dkhil, A. Barthélémy, M. Bibes, *Nat. Mater.* **2014**, *13*, 345.
[9] X. Marti, I. Fina, C. Frontera, J. Liu, P. Wadley, Q. He, R. J. Paull, J. D. Clarkson, J. Kudrnovský, I. Turek, J. Kuneš, D. Yi, J.-H. Chu, C. T. Nelson, L. You, E. Arenholz, S. Salahuddin, J. Fontcuberta, T. Jungwirth, R. Ramesh, *Nat. Mater.* **2014**, *13*, 367.
[10] Y. Liu, L. C. Phillips, R. Mattana, M. Bibes, A. Barthélémy, B. Dkhil, *Nat. Commun.* **2016**, *7*, 11614.
[11] E. O. Chi, W. S. Kim, N. H. Hur, *Solid State Commun.* **2001**, *120*, 307.
[12] K. Takenaka, M. Ichigo, T. Hamada, A. Ozawa, T. Shibayama, T. Inagaki, K. Asano, *Sci. Technol. Adv. Mater.* **2014**, *15*, 15009.
[13] D. Matsunami, A. Fujita, K. Takenaka, M. Kano, *Nat. Mater.* **2014**, *14*, 73.
[14] D. Boldrin, E. Mendive-Tapia, J. Zemen, J. B. Staunton, T. Hansen, A. Aznar, J.-L. Tamarit, M. Barrio, P. Lloveras, J. Kim, X. Moya, L. F. Cohen, *Phys. Rev. X* **2018**, *8*, 041035.
[15] J. Zemen, Z. Gercsi, K. G. Sandeman, *Phys. Rev. B* **2017**, *96*, 024451.
[16] P. Lukashev, R. F. Sabirianov, K. Belashchenko, *Phys. Rev. B* **2008**, *78*, 184414.
[17] G. Gurung, D.-F. Shao, T. R. Paudel, E. Y. Tsymbal, *ArXiv:1901.05040 [Cond-Mat.Mtrl-Sci]* **2019**,.
[18] I. Samathrakis, H. Zhang, *ArXiv:1905.11798 [Cond-Mat.Mtrl-Sci]* **2019**,.
[19] J. Zemen, E. Mendive-Tapia, Z. Gercsi, R. Banerjee, J. B. Staunton, K. G. Sandeman, *Phys. Rev. B* **2017**, *95*, 184438.
[20] D. Boldrin, A. P. Mihai, B. Zou, J. Zemen, R. Thompson, E. Ware, B. V. Neamtu, L. Ghivelder, B. Esser, D. W. McComb, P. Petrov, L. F. Cohen, *ACS Appl. Mater. Interfaces* **2018**, *10*, 18863.
[21] I. E. Dzyaloshinskii, *J. Exptl. Theor. Phys.* **1957**, *33*, 807.

[22] W. Eerenstein, N. D. Mathur, J. F. Scott, *Nature* **2006**, *442*, 759.
[23] L. C. Phillips, R. O. Cherifi, V. Ivanovskaya, A. Zobelli, I. C. Infante, E. Jacquet, N. Guiblin, a. a. Ünal, F. Kronast, B. Dkhil, A. Barthélémy, M. Bibes, S. Valencia, *Sci. Rep.* **2015**, *5*, 10026.
[24] X. Moya, L. E. Hueso, F. Maccherozzi, A. I. Tovstolytkin, D. I. Podyalovskii, C. Ducati, L. C. Phillips, M. Ghidini, O. Hovorka, A. Berger, M. E. Vickers, E. Defay, S. S. Dhesi, N. D. Mathur, *Nat. Mater.* **2012**, *12*, 52.
[25] D. Fruchart, E. F. Bertaut, R. Madar, G. Lorthioir, R. Fruchart, *Solid State Commun.* **1971**, *9*, 1793.
[26] H. Chen, Q. Niu, A. H. MacDonald, *Phys. Rev. Lett.* **2014**, *112*, 017205.
[27] W. Feng, G. Y. Guo, J. Zhou, Y. Yao, Q. Niu, *Phys. Rev. B - Condens. Matter Mater. Phys.* **2015**, *92*, 1.
[28] I. Tomeno, H. N. Fuke, H. Iwasaki, M. Sahashi, Y. Tsonuda, *J. Appl. Phys.* **1999**, *86*, 3853.
[29] E. Krén, G. Kádár, L. Pál, J. Sólyom, P. Szabó, *Phys. Lett.* **1966**, *20*, 331.
[30] D. Boldrin, I. Samathrakis, J. Zemen, A. Mihai, B. Zou, B. Esser, D. McComb, P. Petrov, H. Zhang, L. F. Cohen, *ArXiv:1902.04357 [Cond-Mat.Str-El]* **2019**,.
[31] Y. Sun, C. Wang, L. Chu, Y. Wen, M. Nie, F. Liu, *Scr. Mater.* **2010**, *62*, 686.
[32] D. Boldrin, Z. Gercsi, K. G. Sandeman, T. Hansen, L. F. Cohen, *Inst. Laue-Langevin Doi10.5291/ILL-DATA.5-31-2465* n.d.,.
[33] H. Yan, Z. Feng, S. Shang, X. Wang, Z. Hu, J. Wang, Z. Zhu, H. Wang, Z. Chen, H. Hua, W. Lu, J. Wang, P. Qin, H. Guo, X. Zhou, Z. Leng, Z. Liu, C. Jiang, M. Coey, Z. Liu, *Nat. Nanotechnol.* **2019**,.
[34] D. Fruchart, E. F. Bertaut, J. P. Sénateur, R. Fruchart, *J. Phys. Lettres* **1977**, *38*, 21.

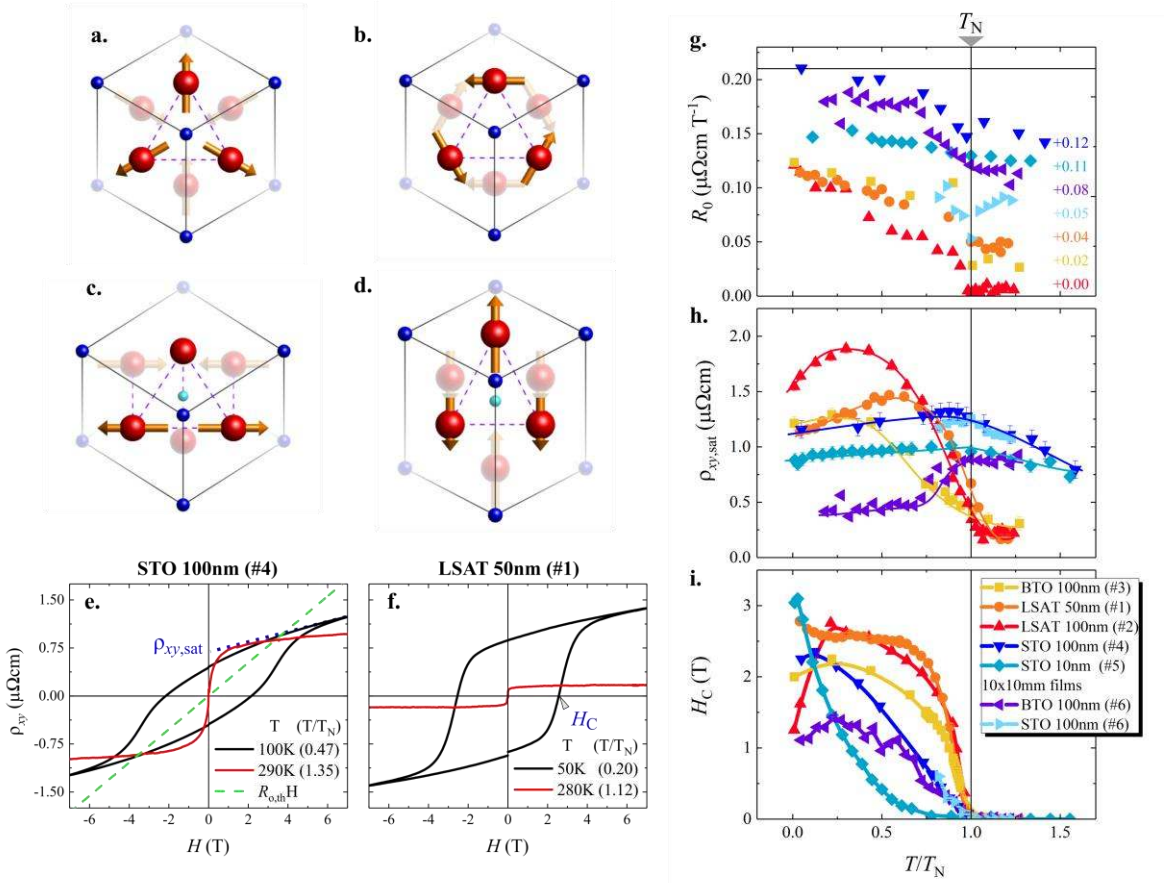

Figure 1. Non-collinear antiferromagnetic structures with (a) Γ_{4g} and (b) Γ_{5g} symmetry. High temperature (c) collinear AFM-Γ_{4g} structure and (d) collinear FIM-Γ_{4g} structures derived from the Γ_{4g} structure of part (a). The equivalent structures derived from the Γ_{4g} structure (part (b)) are predicted to occur in Mn_3GaN under tensile and compressive biaxial strain, respectively [19]. (e-f) Magnetic field dependence of Hall resistivity, ρ_{xy}, measured on Mn_3NiN thin films (e) 100nm on STO (#4) and (f) 50nm on LSAT (#1). The normal Hall contribution estimated from the calculated carrier density, $R_{o,th}$, is also potted in (e). (g) Normal Hall contribution, where the data have been offset along the y-axis for clarity by the amount indicated. The horizontal line indicates the theoretically derived value, $R_{0,th}$; (h) Saturated value of the Hall resistivity, $\rho_{xy,sat}$; (i) Coercive field, H_C; all parts (g-i) plotted as a function of reduced temperature, T/T_N, for all films. The lines are a guide to the eye.

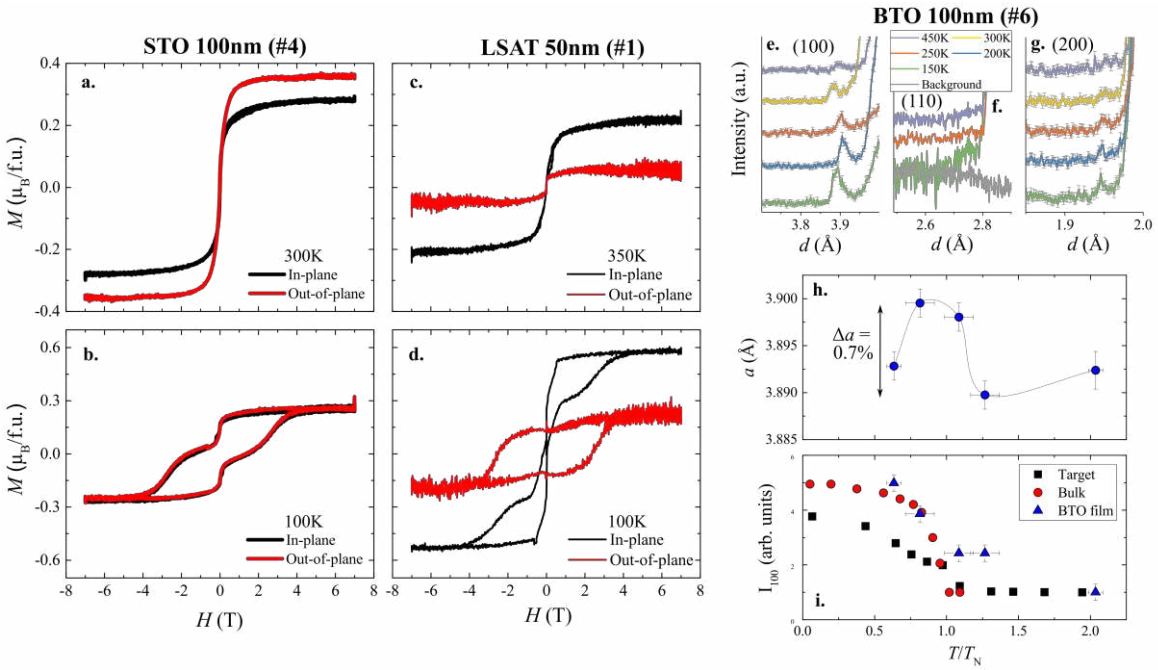

Figure 2. In-plane (IP) and out-of-plane (OOP) magnetisation data for; (a-b) 100nm film on STO (#4) at 300 and 100K, respectively; (c-d) 50nm on LSAT (#1) at 350 and 100K, respectively. A background has been subtracted from all datasets so as to saturate the signal at high field. (e-g) Neutron diffraction measurements of a 100nm Mn_3NiN/BTO film (#6) showing the (e) (100), (f) (110) and (g) (200) peaks. The data have been offset for clarity; (h) Temperature dependence of the *a*-lattice parameter of the film #6. The line is a guide to the eye. (i) Normalised intensity of the (100) peak from the data in (e) as well as a high-quality bulk sample and the ceramic target used for film growth.

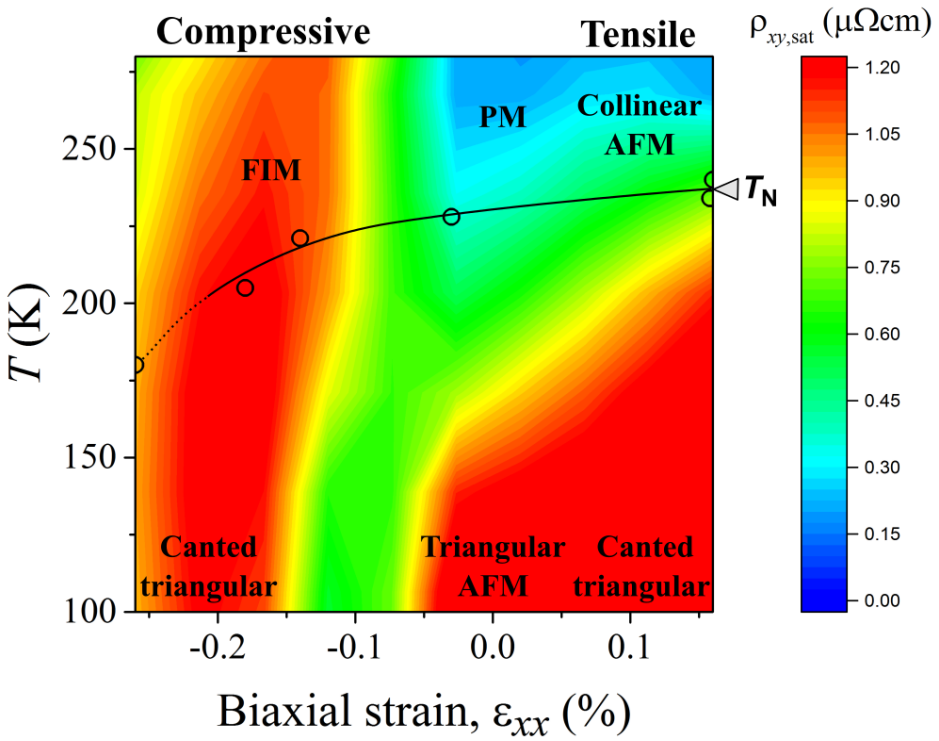

Figure 3. Phase diagram of Mn_3NiN thin films as a function of biaxial strain and temperature. The z-axis is defined by the Hall resistivity, $\rho_{xy,sat}$, which is plotted as a function of temperature for films #1-6, with the strain and T_N values for these films plotted as symbols. The colour scale between these points is interpolated. The black solid (dashed) line indicates a 1st- (2nd-) order transition. The predicted magnetic structures based on the Mn_3GaN phase diagram are shown for each region.

The table of contents entry should be 50–60 words long and should be written in the present tense and impersonal style (i.e., avoid we). The text should be different from the abstract text.

A multi-component magnetic phase diagram induced by biaxial strain is demonstrated in thin films of piezomagnetic Mn_3NiN. Confirming theoretical predictions, regions of high and low magnetisation exist under compressive and tensile strain, respectively. Large and sharp magnetic changes can be achieved by traversing this rich phase diagram, in principle achievable with electric field, opening the field to novel piezospintronic devices based on Mn_3AN materials.

Keyword: piezomagnetism; antiperovskite; ; antiferromagnet; spintronics, frustration

Title: The biaxial strain dependence of magnetic order in spin frustrated Mn_3NiN thin films

ToC figure

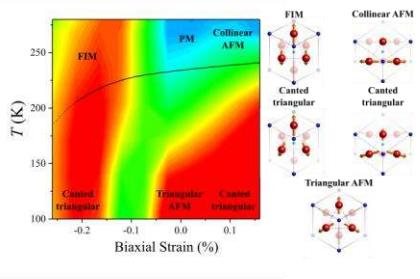
FIM
PM
Collinear AFM
Canted triangular
Triangular AFM
Canted triangular
T (K)
250
200
150
100
-0.2
-0.1
0.0
0.1
Biaxial Strain (%)
FIM
Collinear AFM
Canted triangular
Canted triangular
Triangular AFM

Supporting Information

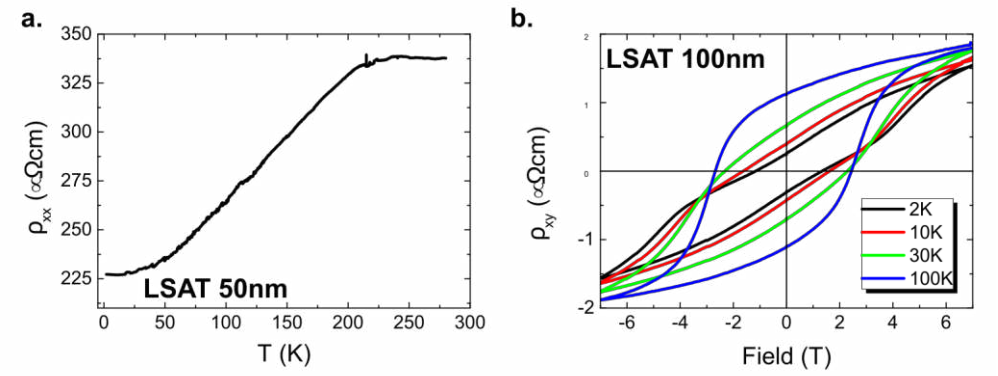

Figure S1: (a) ρ_{xx} as a function of temperature for film #1 (LSAT, 50nm); (b) ρ_{xy} as a function of field for film #2 (LSAT, 100nm) at 4 different temperatures.

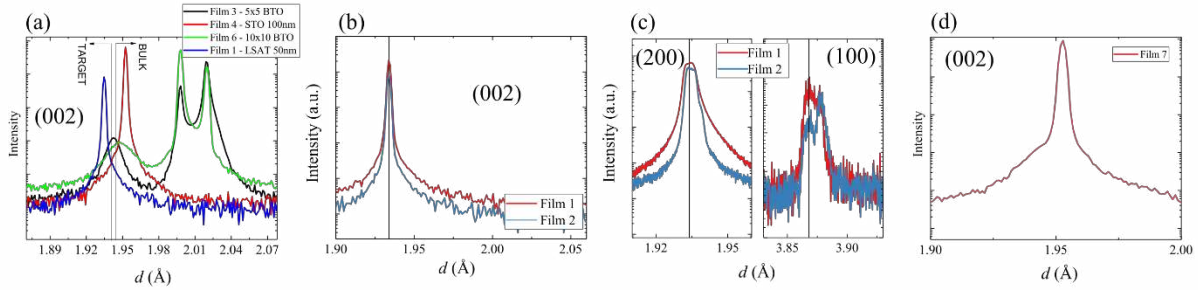

Figure S2: (a) Out-of-plane X-ray diffraction for Mn_3NiN films grown on BTO (#3 and #6), LSAT (#1) and STO (#4) showing the (002) reflection. The bulk and target lattice parameters are marked as verticle lines. (b) Out-of-plane X-ray diffraction for Mn_3NiN films grown on LSAT (#1 and #2) (c) Grazing incidence XRD for the same films in part (b). (d) Out-of-plane X-ray diffraction for Film #7.

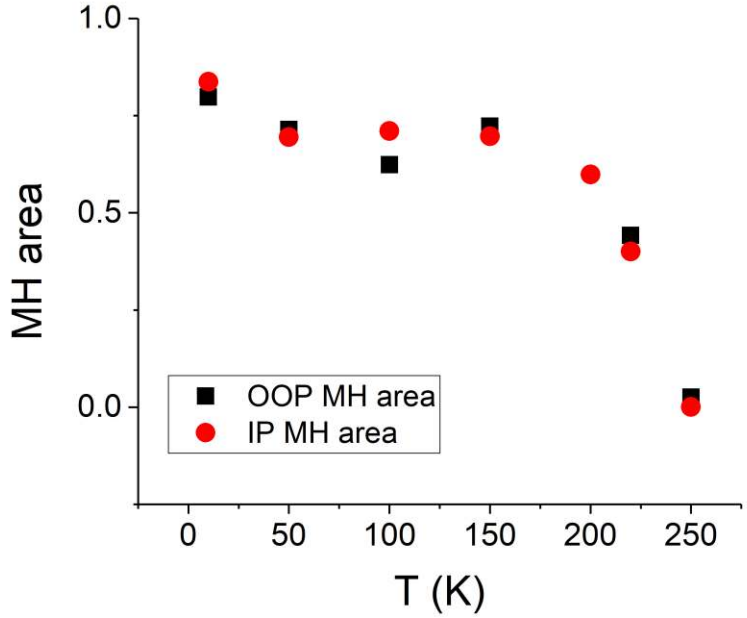

Figure S3: The in-plane and out-of-plane M(H) hysteresis area as a function of temperature for film #1 (LSAT, 50nm).

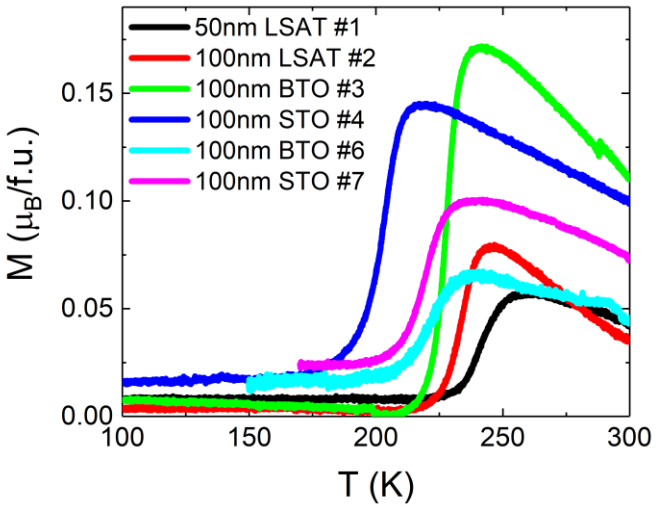

Figure S4: Magnetisation as a function of temperature measured with applied in-plane field H = 0.05T after zero-field-cooling.

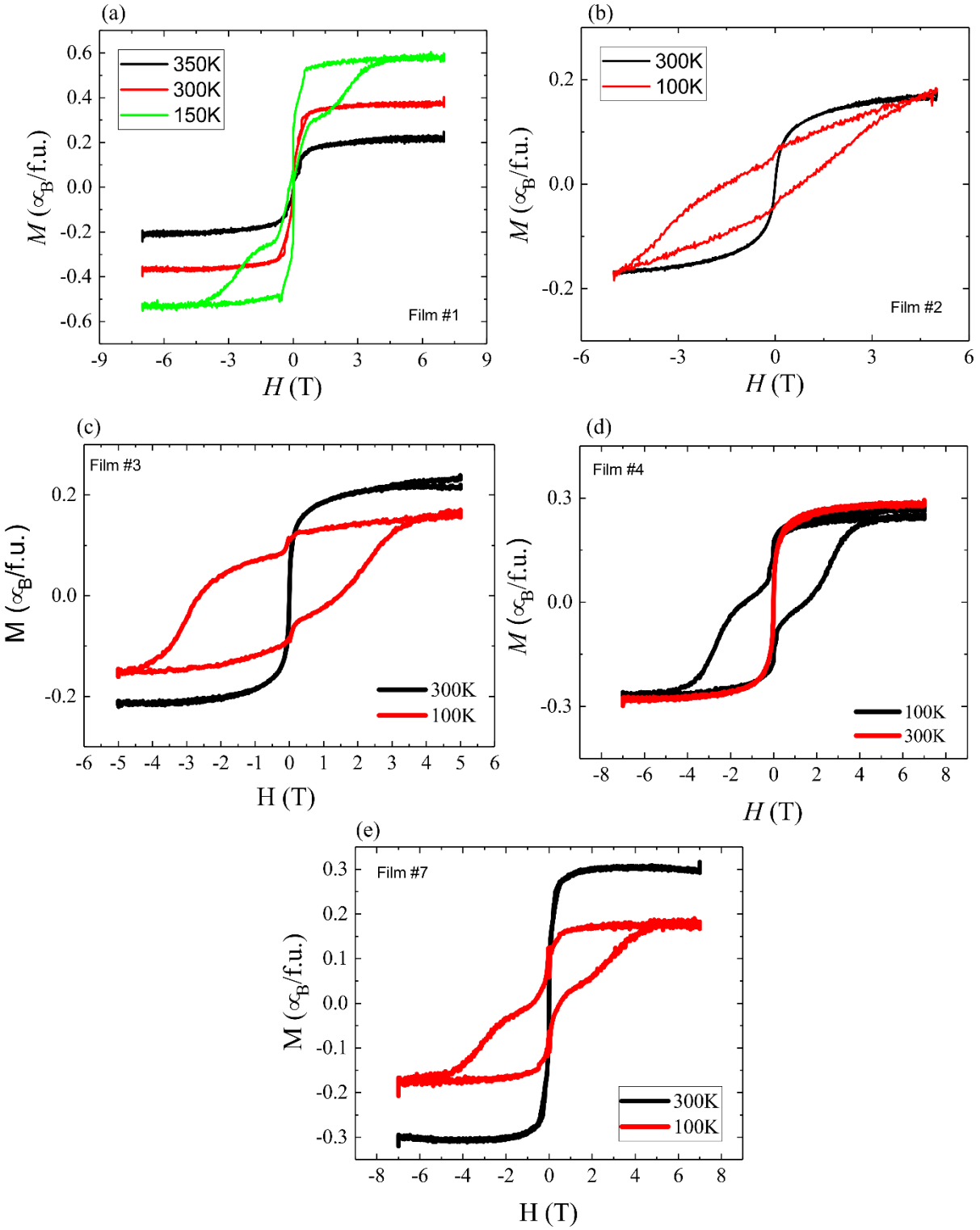

Figure S5: Magnetisation as a function of field measured with the field applied in-plane at temperatures of (a) 350, 300 and 100K and (b-e) 300 and 100K.

Sample #	Film/Substrate	Thickness (nm)	$T_{N,mag}$ (K)	$T_{N,dM/dT}$ (K)	c (Å)	a (Å)	ε_{xx} using υ = 0.41(%)	Measured $\varepsilon_{xx} = \varepsilon_{yy}$ (%)	$\rho_{xx}(290K)$ (μΩcm)	TEM c 30nm (Å)	TEM a 30nm (Å)
1	Mn_3NiN/LSAT 5x5mm	50	250	240	3.865	3.879	0.16	0.12	340		
2	Mn_3NiN/LSAT 5x5mm	100	245	234	3.866	3.876	0.16	0.09	460		
3	Mn_3NiN/BTO 5x5mm	100	240	228	3.883	-	-0.03		500		
4	Mn_3NiN/STO 5x5mm	100	215	205	3.898	-	-0.18	-1.09 30nm	382	3.939	3.838
5	Mn_3NiN/STO 5x5mm	10	180	-	3.905	-	-0.26		190		
6	Mn_3NiN/BTO 10x10mm	100	235	221	3.894	3.887*	-0.09	-0.07	408		
7	Mn_3NiN/STO 10x10mm	100	235	220	3.905	-	-0.26		952		
8	Polycrystalline target	-	235	229	3.8805	3.8805	-		550		

Table S1: **Selected properties of the Mn_3NiN thin films measured in this study. The Néel temperature is determined from magnetometry, either by the peak in M(T) ($T_{N,mag}$) or the peak in dM/dT ($T_{N,dM/dT}$). The c lattice parameter is measured from X-ray diffraction, whilst the biaxial strain $\varepsilon_{xx} = \varepsilon_{yy}$ is calculated from c with Poisson's ratio of 0.41. *Determined from neutron diffraction**